10-1-2021

Intra- and inter-tumoral heterogeneity of liver metastases in a patient with uveal melanoma revealed by single-cell RNA sequencing

Weitao Lin
Edith Cowan University

Aaron Beasley
Edith Cowan University

Nima Mesbah Ardakani

Elena Denisenko

Leslie Calapre
Edith Cowan University

See next page for additional authors

10.1101/mcs.a006111
Lin, W., Beasley, A. B., Ardakani, N. M., Denisenko, E., Calapre, L., Jones, M., ... & Gray, E. S. (2021). Intra-and inter-tumoral heterogeneity of liver metastases in a patient with uveal melanoma revealed by single-cell RNA sequencing. *Molecular Case Studies*, mcs-a006111. https://doi.org/10.1101/mcs.a006111

Intra- and inter-tumoral heterogeneity of liver metastases in a patient with uveal melanoma revealed by single-cell RNA sequencing

Weitao Lin[1,2,3], Aaron B. Beasley[1,2], Nima Mesbah Ardakani[4,5,6], Elena Denisenko[3], Leslie Calapre[2], Matthew Jones[3], Benjamin A. Wood[4,5], Lydia Warburton[1,2,7,8], Alistair R. R. Forrest[3], Elin S. Gray[1,2]*

AFFILIATIONS

[1]Centre for Precision Health, Edith Cowan University, Joondalup, WA 6027, Australia

[2]School of Medical and Health Sciences, Edith Cowan University, Joondalup, WA 6027, Australia

[3]Harry Perkins Institute of Medical Research, QEII Medical Centre and Centre for Medical Research, the University of Western Australia, Nedlands, WA 6009, Australia

[4]Department of Anatomical Pathology, PathWest, QEII Medical Centre, Nedlands, WA 6009, Australia

[5]School of Pathology and Laboratory Medicine, the University of Western Australia, Crawley, WA 6009, Australia

[6]College of Science, Health, Engineering and Education, Murdoch University, Murdoch, WA 6150, Australia

[7]Department of Medical Oncology, Sir Charles Gairdner Hospital, Nedlands, WA 6009, Australia

[8]Department of Medical Oncology, Fiona Stanley Hospital, Murdoch, WA 6150, Australia

*Correspondence: e.gray@ecu.edu.au

Short running title: Heterogeneity of metastases of uveal melanoma

ABSTRACT

Tumour heterogeneity is a major obstacle to the success of cancer treatment. An accurate understanding and recognition of tumour heterogeneity is critical in the clinical management of cancer patients. Here, we utilised single-cell RNA sequencing (scRNA-seq) to uncover the intra- and inter-tumoural heterogeneity of liver metastases from a patient with metastatic uveal melanoma. The two metastases analysed were largely infiltrated by non-cancerous cells with significant variability in the proportion of different cell types. Analysis of copy number variations (CNVs) showed gain of 8q and loss of 6q in both tumours, but loss of chromosome 3 was only detected in one of the tumours. SNP array revealed a uniparental isodisomy 3 in the tumour with two copies of chromosome 3, indicating a re-gain of chromosome 3 during the development of the metastatic disease. In addition, both tumours harboured subclones with additional CNVs. Pathway enrichment analysis of differentially expressed genes revealed that cancer cells in the metastasis with isodisomy 3 showed up-regulation in epithelial-mesenchymal transition and myogenesis related genes. In contrast, upregulation in interferon signalling was observed in the metastasis with monosomy 3 and increased T-cell infiltrate. This study highlights the complexity and heterogeneity of different metastases within an individual case of uveal melanoma.

INTRODUCTION

Uveal melanoma (UM) is the second most common subtype of melanoma. Although the primary UM can be controlled by either surgery or radiation brachytherapy, distant metastases eventually develop in up to 50% of UM patients (Krantz et al. 2017). The liver is the initial metastatic site in the overwhelming majority of cases (95%) (Willson et al. 2001). There is no consensus on the treatment to metastatic UM, and the median overall survival is about 1 year (Khoja et al. 2019; Rantala et al. 2019). Recent results suggest that treatment with tebentafusp or combination immunotherapy using nivolumab and ipilimumab provide some clinical benefit (Middleton et al. 2020; Pelster et al. 2021). However, more effective treatments for metastatic UM are still urgently needed. Once metastatic disease develops, 80% and 92% of the patients die within 1 and 2 years, respectively (Diener-West et al. 2005; Jovanovic et al. 2013). The molecular subtypes of UM have been defined based on their gene expression profile (GEP), chromosome copy number variations (CNVs) and key driving mutations (Onken et al. 2004; Royer-Bertrand et al. 2016; Robertson et al. 2017; Jager et al. 2018; Beasley et al. 2020). Two prognostically favourable subtypes, which have either a low (Group A) or an intermediate (Group B) metastatic risk, are associated with disomy 3 and Class 1 GEP, possess mutations in *EIF1AX* (Group A) or *SF3B1* (Group B), and harbour two (Group A) or more (Group B) copies of chromosome 8q. In contrast, two prognostically unfavourable subtypes, which are associated with a high metastatic risk, show monosomy 3 and Class 2 GEP, inactivation of *BAP1* and an extra copy of chromosome 8q (Group C) or multiple copies of chromosome 8q (Group D). Group D is also associated with significant inflammation and immune infiltrate.

It has been well recognised that tumour heterogeneity poses a significant challenge in the management of cancer patients (Bedard et al. 2013). The heterogeneity of liver metastases in UM is under-investigated due to both rarity of the disease and the fact that surgical removal is not a standard practice for UM patients with liver metastasis. Nonetheless, Krishna and colleagues demonstrated the intersegmental heterogeneity of the immune signatures in UM metastases using bulk analysis (Krishna et al. 2020). In the past decade, single-cell RNA sequencing (scRNA-seq) has been developed as a powerful tool to identify and study tumour heterogeneity (Kolodziejczyk et al. 2015). Here, we characterise the genomic profile of two concurrent liver metastases from a patient with UM using scRNA-seq and copy number alteration analysis. We further compare the molecular results to the clinical characteristics, to exemplify the heterogeneity of metastatic UM tumours.

RESULTS

Clinical presentation

A 69-year-old male was diagnosed with choroidal UM in his left eye in 2014 (labelled as week 0) and was enrolled in our study prior to Iodine^{125} plaque insertion (Figure 1A). The patient was followed up clinically with direct eye examination for local surveillance and six-monthly positron emission tomography (PET) scans to monitor for metastatic disease. An isolated liver lesion (56 mm) in segment III was identified on imaging during his follow-up. The patient underwent a partial liver resection of this lesion at week 165. Histopathology confirmed metastatic uveal melanoma. Postoperatively, he had no other identified metastases and re-commenced active surveillance. At week 202, he underwent

enucleation of the left eye due to local recurrence. At week 246, an intensely FDG-avid liver lesion was identified in the left lateral liver segment by PET (Figure 1B). At week 253, the patient underwent a second operation, during which several variably pigmented abnormal nodules were identified macroscopically, ranging from less than 1 to 17 mm in maximum diameter. Two separate metastatic lesions were resected, providing the specimens described here. After surgery, a restaging PET scan at week 255 indicated further liver metastases in segment VIII and segment VI/VII, which were not previously evident. The patient was commenced on combination immunotherapy with ipilimumab and nivolumab at week 256, but only completed two doses due to the development of grade III immune-related hepatitis. Liver toxicity improved but did not completely dissipate with high dose steroids, therefore, mycophenolate was added. A restaging scan at week 266 showed marked hepatomegaly and upper abdominal disease in addition to two new bone metastases. At week 267, therapy continued with single-agent nivolumab only for three more cycles and the patient died soon after from advanced metastatic UM.

Histopathological characteristics

The enucleated left eye at week 202 contained a large choroidal melanoma (14 × 6 mm), predominantly composed of epithelioid cells according to Callender classification. The tumour was partly necrotic with evidence of radiation-induced tumour reduction/necrosis affecting approximately 40% of the total tumour volume. There was also evidence of trans-scleral invasion (to conjunctival stroma). The optic nerve margin was uninvolved.

Representative samples for the two metastatic nodules resected from the left lateral liver segment at week 253 were harvested for molecular studies and labelled as WL02 and WL03. Histopathological examination revealed that the tumour cells in WL02 were composed of a combination of spindle and epithelioid cells, while the tumour cells in WL03 had a purely epithelioid appearance (Figure 1C). Both WL02 and WL03 consisted of tumour cells showing enlarged pleomorphic round to oval nuclei, often prominent nucleoli and moderately abundant eosinophilic cytoplasm with varying melanin pigmentation. A variable number of admixed lymphocytes, macrophages and stromal cells (including hepatic stellate cells) were present in the milieu surrounding these nodules, with the WL02 sample showing widespread areas with an oedematous stroma containing a high proportion of stromal cells and macrophages while WL03 contained areas rich in lymphocytes, particularly at the interface between the tumour and native liver tissue.

Genomic analysis

A tissue sample of the primary tumour was analysed at the time of radiation plaque insertion by multiplex ligation-dependent probe amplification (MLPA) (Supplementary Figure 1A). The tumour was suggested to be of high metastatic risk based on the cytogenetic findings including loss of chromosome 1p, loss of chromosome 3 and gain of chromosome 8q.

WL02 and WL03 metastatic nodules were analysed using droplet-based scRNA-seq. After quality control, a total of 1,225 and 5,116 high-quality single cells were recovered from WL02 and WL03, respectively. Based on the expression of a panel of canonical marker genes, all the cells were manually

annotated into 11 groups (Figure 2A). Both tumours were heavily infiltrated by non-neoplastic cells (76.73% vs 82.86%) including hepatic stellate cells (HSCs) and immune cells, with tumour cells constituting 17-23% of the cells sequenced (Figure 2B). The two tumours differed in the proportion of non-tumour cell types in their microenvironment, with WL03 presenting a large T-cell infiltrate (54%). WL02 was enriched in HSCs (36%) and endothelial cells (7%) compared to WL03, which only had a low percentage of both cell types (1.9% of each). Both tumours contained a similar number of macrophages (9.71% vs 9.77%). Tumour cells in WL02 were more proliferative as evidenced by high proportion of cells in S and G2M phases, while WL03 manifested quiescent characteristic with a high proportion of tumour cells in G1 phase (Figure 2C).

Comparison of tumour cells in WL02 and WL03 by gene set enrichment analysis (GSEA) indicated that genes involved in epithelial-mesenchymal transition (EMT), myogenesis, coagulation and hypoxia were significantly enriched in WL02 (Figure 2D). Conversely, genes involved in immune-related pathways such as interferon gamma and alpha response were significantly enriched in WL03, which was consistent with the high abundance of T cell infiltrate observed in this tumour (Figure 1C and 2B).

We examined CNVs in the tumour cells from these two metastases using inferCNV (Figure 3A). Hierarchical clustering indicated gain of 8q and loss of 6q in both tumours consistent with the primary tumour genotype, but loss of chromosome 3 was only apparent in WL03. The main CNV profile identified by inferCNV, including gain of 8q and loss of 6q in both tumours, and loss of chromosome 3 in WL03, was confirmed by low pass whole genome sequencing (LP-WGS) (Figure 3B) and by array comparative genomic hybridisation (aCGH) (Supplementary Figure 1B). Targeted sequencing revealed in *BAP1* E182V mutation in both WL02 and WL03.

In addition, inferCNV revealed the development of subclones within each tumour whereas a subclone (clone K) carrying gains of 5q,15p and 21 was found within WL02, while a subclone (clone I) carrying gain of 2p was found within WL03 (Figure 3C). These analyses also indicated several distinct CNVs between these two tumours, with gain of 7p, partial gain and loss of 11q uniquely observed in WL02. Conversely, gains of 1q, 4p, 6p and 16p, and loss of 16q were found in WL03, but were not evident in WL02.

Overall, the major discordance between the two tumours was the lack of monosomy 3 in WL02. SNP array analysis indicated uniparental isodisomy of chromosome 3 in WL02 (Figure 3D). Isodisomy 3 in WL02 did not reconstitute the expression of *BAP1*, indicated by the lack of mRNA expression (Supplementary Figure 2A), further validated by the lack of BAP1 expression in the corresponding formalin-fixed paraffin-embedded (FFPE) blocks (Figure 4A). However, GEP of a few genes was slightly shifted in tumour cells from WL02 compared with WL03. These included expression of *CDH1*, *ECM1*, *EIF1B*, *FXR1* and *HTR2B,* which are associated with UM risk classification, suggesting gene expression profile trend towards a Class 1 GEP subtype (Figure 4B).

DISCUSSION

The results of the presented study demonstrated a significant inter- and intra-tumour heterogeneity in two spatially separated liver metastases of UM at the single-cell level. Tumour cells in WL02 showed migratory properties with an enrichment of genes involved in EMT, myogenesis, coagulation and

hypoxia. These cells were also found to be in an active proliferative state. Altogether this suggests a high migratory and invasive propensity, which was further supported by the evidence of widespread metastases detected in other liver segments, lymph node and bone in subsequent PET scans.

Our analysis shows that cells from a primary tumour with monosomy 3 could re-gain a copy of this chromosome in the form of isodisomy 3 in all tumour cells in one of its metastatic deposits, and not the other. The lack of BAP1 expression in the presence of 2 copies of chromosome 3 in this metastatic deposit suggests duplication of the chromosome harbouring an inactivating mutation in *BAP1* allele. Loss of BAP1 expression is associated with a Class 2 GEP (Harbour et al. 2010; Robertson et al. 2017), and a recent study demonstrated that the reintroduction of a wild-type BAP1 copy *in vitro* could shift the GEP towards a Class 1 subtype (Karlsson et al. 2020). Conversely, it can be speculated that isodisomy 3 without a functional BAP1 in WL02 could still partially reverse the GEP to a Class 1 subtype, if there were other factors on chromosome 3 which were involved in the regulation of the GEP. It is unclear how chromosome 3 duplication may benefit disease progression once metastatic disease is stablished. However, it could represent a lack of pressure to maintain a Class 2 GEP at the late stage of the disease. Notably, isodisomy 3 as well as losses of 1p, 6q and gains of 1q, 8q have been reported to be acquired during the metastatic stage (Rodrigues et al. 2019), suggesting that restoration of heterozygosity may provide a selective advantage at the metastatic stage.

Loss of chromosome 9p has been observed in a quarter of UM (Harbour 2012), similarly, our analysis showed a loss of chromosome 9 in WL02 (**Figure 3B**). Chromosome 9p loss has been associated with loss of *CDKDN2*, resulting in a higher proliferative state of tumour cells as observed in WL02, implied by the cell-cycle scoring analysis. Interestingly, we also found that WL02 harboured the loss of chromosome 9, concurrently having a higher level of 8q gain, which is consistent with the proposed evolutive pattern of metastatic UM (Shain et al. 2019).

In a recent study, Pandiani *et al*. used scRNA-seq to study intra-tumoural heterogeneity in primary UM (Pandiani et al. 2021), and demonstrated the critical role of HES6 in enhancing growth and motile ability of primary UM. Our data showed increased expression of *HES6* in both liver metastases (Supplementary Figure 2B). However, the tumour (WL02) with more proliferative and motile characteristics had a lower *HES6* expression, suggesting that this metastatic tumour might have relied on alternative signalling to promote proliferation and migration.

A recent study in cutaneous melanoma demonstrated that CNVs can influence the local immune composition and chromosome 7 gain was attributed to a low leukocyte infiltrate in the tumour microenvironment (Mitra et al. 2020). In agreement with this study, WL02 harbouring a gain of 7p showed a lower T-cell density compared to WL03. Concomitantly, WL02 had a large proportion of HSCs infiltrate. As demonstrated in a previous study (Yu et al. 2004), HSCs can suppress T-cell infiltration, suggesting that HSCs may have also affected the reduced T cell composition in this sample. These observations signify a potential differential sensitivity in response to immune checkpoint inhibitors in these two separate tumours.

The expression of immune checkpoint proteins in T cells in both tumour was consistent with the previous studies (Supplementary Figure 2C) (Durante et al. 2020; Karlsson et al. 2020). T cells did not express *HAVCR2* (TIM-3) or *PDCD1* (PD-1). The latter could explain why nivolumab, after discontinuation of

combination immunotherapy, was ineffective in this patient. On the other hand, *LAG3* was strongly expressed in T cells in WL03, but not in T cells in WL02. This heterogeneity amongst UM metastatic deposits may have future therapeutic implications as LAG3 blockade is pursued as promising treatment for cancer (Atkinson et al. 2020).

In summary, this case study highlights the complexity of UM liver metastases, broadening the spectrum of transcriptome landscape in such tumours at a single-cell level. More importantly, it emphasises the significance of an accurate assessment of inter- and intra-tumoural heterogeneity for delivering the most specific and personalised therapeutic intervention at the right time for patients.

METHODS

Patient and Sample Collection

Resected tumours were triaged by pathologist immediately after surgery and immersed into RPMI 1640 supplemented with 20% foetal bovine serum, 10,000 U/mL penicillin and 10,000 µg/mL streptomycin (ThermoFisher Scientific) at 4°C to maximise the viability of cells. A fraction of each tumour was freshly subjected to single-cell dissociation while the rest was processed as FFPE blocks for histopathology analysis.

Preparation of Single-cell Suspension

Tumours obtained from the surgery were freshly subjected to single-cell dissociation using Human Tumour Dissociation Kit (Miltenyi Biotec) according to the manufacturer's instructions. Briefly, the tumours were washed with plain RPMI (ThermoFisher Scientific) supplemented with Penicillin and Streptomycin (ThermoFisher Scientific), and processed into pieces (1 mm^3) using scalpels with the recommended volume of enzyme mix as per instructions. The tumour pieces and enzyme mix were then transferred into gentleMACS™ C tubes (Miltenyi Biotec), and then the tubes were loaded onto the gentleMACS™ Octo Dissociator with Heaters (Miltenyi Biotec) with the program according to the manufacturer's instructions. After incubation, digested tissues were filtered through Falcon® 70-µm strainers (Corning) and washed. Cell suspension was further filtered through 40-µm strainers to remove cell clumps. The viability was assessed by ReadyProbe® Cell Viability Imaging Kit (ThermoFisher Scientific) to ensure the viability was greater than 90%.

Single-Cell RNA Sequencing and Analysis

Single-cell RNA sequencing was performed using Chromium Single Cell 3' Reagent Kits v3 (10x Genomics) according to the manufacturer's protocol. WL02 was aimed with a targeted capture of 2,000 cells due to the limited tissue obtained from the surgery, while WL03 with a targeted capture of 9,000 cells. Gel Beads-in-emulsion was generated using Chromium Single Cell B Chip Kit. Libraries were sequenced using the Illumina NovaSeq 6000 and S2 flow cells (100 cycle kit) with a read one length of 28 cycles and a read two length of 94 cycles.

Raw data was processed as described previously (Denisenko et al. 2020). Briefly, BCL files were demultiplexed and converted into FASTQ using bcl2fastq utility of Illumina BaseSpace Sequence Hub. FASTQ files were processed using Cell Ranger 3.0.2 with refdata-cellranger-GRCh38-3.0.0 reference. Raw gene-barcode matrices from Cell Ranger output were used for downstream processing. Cells were distinguished from background noise using EmptyDrops (Lun et al. 2019). Outlier cells with high ratio

of number of detected UMI to genes (> 3 median absolute deviations from median) were removed using Scater (McCarthy et al. 2017). The pre-processed data from these two tumours was then integrated in R (version 3.6.2) (Team 2013) with the SCTransform workflow using Seurat toolkit (version 3.2.3) (Stuart et al. 2019). Quality control was performed by retaining cells with nCount_RNA greater than 400, nFeature_RNA greater than 100 but less than 8000, and mitochondrial content less than 10 percent. CellCycleScoring() function was used to predict the phases of each cell according to Seurat tutorial. In SCTransform() function, percent of mitochondrial content was used in "vars.to.regress" argument to regress out variation. In FindIntegrationAnchors() function, WL02 was used as a reference dataset as it contained less doublets. The first 30 principal components were used in RunUMAP() and FindNeighbors() functions, while the resolution parameter was set to 2 in FindCluster() function. For other parameters unspecified above, default values were used in the SCTransform workflow.

Clusters were visualised in a two-dimensional unified manifold approximation and projection (UMAP) and were annotated using canonical marker genes based on literature (MacParland et al. 2018; Durante et al. 2020; Sharma et al. 2020; Zhao et al. 2020). The marker genes were as listed below: tumour cells (*MLANA*, *MITF*, *DCT*), hepatic stellate cells (*ACTA2*, *COL1A1*, *COL1A2*, *TAGLN*, *COL3A1*, *RBP1*, *SPARC*), endothelial cells (*PECAM1*, *VWF*), NK cells (*KLRF1*), T cells (*CD3D*), B cells (*CD19*, *CD79A*, *MS4A1*), Plasma cells (*IGHG1*, *MZB1*, *SDC1*, *CD79A*), plasmacytoid dendritic cells (*LILR4*, *GZMB*), dendritic cells (*CLEC9A*, *CD1C*, *CD1E*), monocytes (*S100A8*, *S100A9*, *S100A12*), and macrophages (*CD163*, *IL10*, *C1QA*, *C1QB*, *C1QC*).

GSEA

To obtain differentially expressed genes in tumour cells between WL02 and WL03, FindMarkers() function from Seurat package (version 3.2.3) was used (Stuart et al. 2019). GSEA software (version 4.1.0, http://www.gsea-msigdb.org/gsea/downloads.jsp) for Linux was used to calculate hallmark gene set enrichment (h.all.v7.2.symbols.gmt) using GSEAPreanked and Log2 fold change. Hallmark normalised enrichment score (NES) was plotted against enriched pathways using R (version 4.0.4).

CNV Analysis

InferCNV (version 1.7.1) was used to predict the copy number variations from scRNA-seq data (InferCNV of the Trinity CTAT Project: https://github.com/broadinstitute/InferCNV). To keep high-quality T cells as normal reference cells, only T cells that had no expression of *PRAME*, *HTR2B*, *MLANA* and *MITF*. A value of 0.1 was used for the "cutoff" argument and default values were used in other unspecified arguments. Intra-tumour evolutionary trees were generated using UPyhloplot2 (version 2.3; https://github.com/harbourlab/uphyloplot2) as described (Kurtenbach et al. 2020). Phylogenetic tree was manually annotated using the output of UPhyloplot2 and ".pred_cnv_regions.dat" file from InferCNV in Adobe Illustrator (version 25.2.3).

Shallow LP-WGS was used to detect CNVs from WL02 and WL03. DNA was extracted from FFPE tissue using the AllPrep DNA/RNA Mini Kit (Qiagen). 100ng of DNA was digested using the MseI restriction enzyme (New England Biolabs) and 200 bp libraries constructed using the NEBNext Fast DNA Library Prep Set for Ion Torrent (New England Biolabs) to manufacturers specifications. Resultant DNA was templated and loaded into an Ion 540 chip (ThermoFisher Scientific) at 60 pM using the Ion

Chef (Thermofisher Scientific). Libraries were sequenced on an Ion S5 (ThermoFisher Scientific) for 520 flows. Data was uploaded and analysed using Ion Reporter (version 5.14).

CGH and SNP arrays were performed in the same FFPE derived DNA samples. For CGH assay, the test DNA and sex mismatched human reference DNA were differentially labelled with fluorophores. Equal quantities of the 2 DNA samples were mixed and hybridised onto a SurePrint G3 Human CGH Microarray, 8 × 60K (Agilent) and digitally scanned to capture and quantify the relative fluorescence intensities. The ratio of the fluorescence intensities was analysed by CytoGenomics software (Agilent) for further analysis and detection of potential CNVs. For SNP array the Infinium HD assay was performed utilising Illumina iScan and HumanCytoSNP FFPE-12 BeadChip array according to the manufacturer's protocol (Illumina, USA). The BeadChips were stained, and then imaged, using a BeadArray Reader (Illumina). Image data were analysed with GenomeStudio (Illumina).

ADDITIONAL INFORMATION

Data availability

The scRNA-seq data generated in this study has been deposited in Gene Expression Omnibus (GEO) under accession code GSE176029.

Ethics statement

This study was approved by the Human Research Ethics Committee protocols from Edith Cowan University (No. 11543) and Sir Charles Gairdner Hospital (No. 2013-246) in compliance with the Declaration of Helsinki. Experiments were performed in accordance with institutional and national guidelines and regulations. The patient provided signed informed consent for the collection of specimens, detailed analyses of the derived genetic material and access to clinical data.

Acknowledgements

We are grateful to the patient who donated the samples in this research. We thank Dr Bryon Jaques at Sir Charles Gairdner Hospital who performed the surgery to collect the tumour samples, Professor Helen Rizos at Macquarie University who shared the methods of tumour dissociation, Dr Zeyad Al-Ogaili at Fiona Stanley Hospital who calculated the total lesion glycolysis of the PET scan, Dr Cleo Robinson and Dr Karen Woodward from PathWest for CGH and SNP array analyses. We also thank Mr Michael A. Durante and Professor J. William Harbour at Bascom Palmer Eye Institute for the discussion of this project.

Author Contributions

W.L., A.B., N.M.A. and E.S.G wrote the manuscript. W.L. prepared the libraries for scRNA-seq. M.J. carried out the Novaseq sequencing. L.C. prepared the libraries and performed the LP-WGS. W.L., A.B. and E.D. carried out the bioinformatic analysis. L.W. recruited the patient and reviewed the clinical history. N.M.A and B.A.W. performed the histopathological analysis. A.R.R.F. and E.S.G. designed and supervised the study. All authors have read and approved the final manuscript.

Funding

This project was supported by the Cancer Research Trust and Cancer Council Western Australia (CCWA) through the 'Enabling advanced single cell cancer genomics in WA' grant to A.R.R.F, and a Collaborative CCWA grant to W.L, N.M.A. and E.D. Genomic data was generated at the Australian

Cancer Research Foundation Centre for Advanced Cancer Genomics. Analysis was made possible with computational resources provided by the Pawsey Supercomputing Centre with funding from the Australian Government and the Government of Western Australia. A.R.R.F. is supported by an Australian National Health and Medical Research Council (NHMRC) Fellowship APP1154524. L.W. is supported by an NHMRC Scholarship APP1190643. A.B.B. is supported by an Edith Cowan University Postgraduate Scholarship and a CCWA PhD Top-up Scholarship. E.S.G. is supported by a CCWA Fellowship.

REFERENCES

Atkinson V, Khattak A, Haydon A, Eastgate M, Roy A, Prithviraj P, Mueller C, Brignone C, Triebel F. 2020. Eftilagimod alpha, a soluble lymphocyte activation gene-3 (LAG-3) protein plus pembrolizumab in patients with metastatic melanoma. *Journal for immunotherapy of cancer* **8**(2).

Beasley AB, Bentel J, Allcock RJ, Vermeulen T, Calapre L, Isaacs T, Ziman MR, Chen FK, Gray ES. 2020. Low-Pass Whole-Genome Sequencing as a Method of Determining Copy Number Variations in Uveal Melanoma Tissue Samples. *The Journal of Molecular Diagnostics* **22**(3): 429-434.

Bedard PL, Hansen AR, Ratain MJ, Siu LL. 2013. Tumour heterogeneity in the clinic. *Nature* **501**(7467): 355-364.

Denisenko E, Guo BB, Jones M, Hou R, de Kock L, Lassmann T, Poppe D, Clement O, Simmons RK, Lister R et al. 2020. Systematic assessment of tissue dissociation and storage biases in single-cell and single-nucleus RNA-seq workflows. *Genome Biol* **21**(1): 130.

Diener-West M, Reynolds SM, Agugliaro DJ, Caldwell R, Cumming K, Earle JD, Hawkins BS, Hayman JA, Jaiyesimi I, Jampol LM et al. 2005. Development of metastatic disease after enrollment in the COMS trials for treatment of choroidal melanoma: Collaborative Ocular Melanoma Study Group Report No. 26. *Arch Ophthalmol* **123**(12): 1639-1643.

Durante MA, Rodriguez DA, Kurtenbach S, Kuznetsov JN, Sanchez MI, Decatur CL, Snyder H, Feun LG, Livingstone AS, Harbour JW. 2020. Single-cell analysis reveals new evolutionary complexity in uveal melanoma. *Nat Commun* **11**(1): 496.

Harbour JW. 2012. The genetics of uveal melanoma: an emerging framework for targeted therapy. *Pigment cell & melanoma research* **25**(2): 171-181.

Harbour JW, Onken MD, Roberson ED, Duan S, Cao L, Worley LA, Council ML, Matatall KA, Helms C, Bowcock AM. 2010. Frequent mutation of BAP1 in metastasizing uveal melanomas. *Science* **330**(6009): 1410-1413.

Jager MJ, Brouwer NJ, Esmaeli B. 2018. The cancer genome atlas project: An integrated molecular view of uveal melanoma. *Ophthalmology* **125**(8): 1139-1142.

Jovanovic P, Mihajlovic M, Djordjevic-Jocic J, Vlajkovic S, Cekic S, Stefanovic V. 2013. Ocular melanoma: an overview of the current status. *Int J Clin Exp Pathol* **6**(7): 1230-1244.

Karlsson J, Nilsson LM, Mitra S, Alsen S, Shelke GV, Sah VR, Forsberg EMV, Stierner U, All-Eriksson C, Einarsdottir B et al. 2020. Molecular profiling of driver events in metastatic uveal melanoma. *Nat Commun* **11**(1): 1894.

Khoja L, Atenafu E, Suciu S, Leyvraz S, Sato T, Marshall E, Keilholz U, Zimmer L, Patel S, Piperno-Neumann S. 2019. Meta-analysis in metastatic uveal melanoma to determine progression

free and overall survival benchmarks: an international rare cancers initiative (IRCI) ocular melanoma study. *Annals of Oncology* **30**(8): 1370-1380.

Kolodziejczyk AA, Kim JK, Svensson V, Marioni JC, Teichmann SA. 2015. The technology and biology of single-cell RNA sequencing. *Mol Cell* **58**(4): 610-620.

Krantz BA, Dave N, Komatsubara KM, Marr BP, Carvajal RD. 2017. Uveal melanoma: epidemiology, etiology, and treatment of primary disease. *Clin Ophthalmol* **11**: 279-289.

Krishna Y, Acha-Sagredo A, Sabat-Pośpiech D, Kipling N, Clarke K, Figueiredo CR, Kalirai H, Coupland SE. 2020. Transcriptome Profiling Reveals New Insights into the Immune Microenvironment and Upregulation of Novel Biomarkers in Metastatic Uveal Melanoma. *Cancers* **12**(10): 2832.

Kurtenbach S, Rodriguez DA, Durante MA, Harbour JW. 2020. UPhyloplot2: Visualizing Phylogenetic Trees from Single-Cell RNA-seq Data. *bioRxiv*: 2020.2005.2025.115550.

Lun AT, Riesenfeld S, Andrews T, Gomes T, Marioni JC. 2019. EmptyDrops: distinguishing cells from empty droplets in droplet-based single-cell RNA sequencing data. *Genome biology* **20**(1): 1-9.

MacParland SA, Liu JC, Ma XZ, Innes BT, Bartczak AM, Gage BK, Manuel J, Khuu N, Echeverri J, Linares I et al. 2018. Single cell RNA sequencing of human liver reveals distinct intrahepatic macrophage populations. *Nat Commun* **9**(1): 4383.

McCarthy DJ, Campbell KR, Lun AT, Wills QF. 2017. Scater: pre-processing, quality control, normalization and visualization of single-cell RNA-seq data in R. *Bioinformatics* **33**(8): 1179-1186.

Middleton MR, McAlpine C, Woodcock VK, Corrie P, Infante JR, Steven NM, Evans TRJ, Anthoney A, Shoushtari AN, Hamid O. 2020. Tebentafusp, A TCR/Anti-CD3 Bispecific Fusion Protein Targeting gp100, Potently Activated Antitumor Immune Responses in Patients with Metastatic Melanoma. *Clinical Cancer Research* **26**(22): 5869-5878.

Mitra A, Andrews MC, Roh W, De Macedo MP, Hudgens CW, Carapeto F, Singh S, Reuben A, Wang F, Mao X et al. 2020. Spatially resolved analyses link genomic and immune diversity and reveal unfavorable neutrophil activation in melanoma. *Nat Commun* **11**(1): 1839.

Onken MD, Worley LA, Ehlers JP, Harbour JW. 2004. Gene expression profiling in uveal melanoma reveals two molecular classes and predicts metastatic death. *Cancer research* **64**(20): 7205-7209.

Pandiani C, Strub T, Nottet N, Cheli Y, Gambi G, Bille K, Husser C, Dalmasso M, Beranger G, Lassalle S et al. 2021. Single-cell RNA sequencing reveals intratumoral heterogeneity in primary uveal melanomas and identifies HES6 as a driver of the metastatic disease. *Cell Death Differ*.

Pelster MS, Gruschkus SK, Bassett R, Gombos DS, Shephard M, Posada L, Glover MS, Simien R, Diab A, Hwu P. 2021. Nivolumab and ipilimumab in metastatic uveal melanoma: results from a single-arm phase II study. *Journal of Clinical Oncology* **39**(6): 599-607.

Rantala ES, Hernberg M, Kivelä TT. 2019. Overall survival after treatment for metastatic uveal melanoma: a systematic review and meta-analysis. *Melanoma research* **29**(6): 561.

Robertson AG, Shih J, Yau C, Gibb EA, Oba J, Mungall KL, Hess JM, Uzunangelov V, Walter V, Danilova L et al. 2017. Integrative Analysis Identifies Four Molecular and Clinical Subsets in Uveal Melanoma. *Cancer Cell* **32**(2): 204-220 e215.

Rodrigues M, Mobuchon L, Houy A, Alsafadi S, Baulande S, Mariani O, Marande B, Rais KA, Van der Kooij MK, Kapiteijn E. 2019. Evolutionary routes in metastatic uveal melanomas depend on MBD4 alterations. *Clinical Cancer Research* **25**(18): 5513-5524.

Royer-Bertrand B, Torsello M, Rimoldi D, El Zaoui I, Cisarova K, Pescini-Gobert R, Raynaud F, Zografos L, Schalenbourg A, Speiser D et al. 2016. Comprehensive Genetic Landscape of Uveal Melanoma by Whole-Genome Sequencing. *Am J Hum Genet* **99**(5): 1190-1198.

Shain AH, Bagger MM, Yu R, Chang D, Liu S, Vemula S, Weier JF, Wadt K, Heegaard S, Bastian BC. 2019. The genetic evolution of metastatic uveal melanoma. *Nature genetics* **51**(7): 1123-1130.

Sharma A, Seow JJW, Dutertre CA, Pai R, Bleriot C, Mishra A, Wong RMM, Singh GSN, Sudhagar S, Khalilnezhad S et al. 2020. Onco-fetal Reprogramming of Endothelial Cells Drives Immunosuppressive Macrophages in Hepatocellular Carcinoma. *Cell* **183**(2): 377-394 e321.

Stuart T, Butler A, Hoffman P, Hafemeister C, Papalexi E, Mauck WM, 3rd, Hao Y, Stoeckius M, Smibert P, Satija R. 2019. Comprehensive Integration of Single-Cell Data. *Cell* **177**(7): 1888-1902 e1821.

Team RC. 2013. R: A language and environment for statistical computing.

Willson JK, Albert DM, Diener-West M, McCaffrey L, Moy CS, Scully RE. 2001. Assessment of metastatic disease status at death in 435 patients with large choroidal melanoma in the collaborative ocular melanoma study (coms) coms report no. 15. *Arch Ophthalmol* **119**(5): 670-676.

Yu MC, Chen CH, Liang X, Wang L, Gandhi CR, Fung JJ, Lu L, Qian S. 2004. Inhibition of T-cell responses by hepatic stellate cells via B7-H1-mediated T-cell apoptosis in mice. *Hepatology* **40**(6): 1312-1321.

Zhao J, Zhang S, Liu Y, He X, Qu M, Xu G, Wang H, Huang M, Pan J, Liu Z et al. 2020. Single-cell RNA sequencing reveals the heterogeneity of liver-resident immune cells in human. *Cell Discov* **6**: 22.

FIGURE LEGENDS

Figure 1. The patient's clinical information.

(A) Treatment history of the patient. (B) An intensely FDG-avid liver lesion (white arrows) was identified in the left lateral segment by PET in week 246. The total lesion glycolysis was equal to 84 SUV × cm^3. (C) H&E staining of two liver metastases WL02 and WL03. Tumour cells in WL02 (left) had a spindled to epithelioid appearance with a relatively high number of admixed stromal cells in an oedematous stroma, while tumour cells in WL03 (right) had an epithelioid appearance and the stroma was rich in lymphocytes at the periphery of the tumour (H&Es, original magnification both ×350).

Figure 2. Aggregate analysis of 6,341 single cells from two liver metastases.

(A) UMAP plot of 6,341 single cells, coloured by cell types that were manually assigned to cell clusters. (B) Pie chart of each liver metastasis showing the percentages of annotated cell types. (C) Cell cycle distribution of tumour cells. Percentage of tumour cells in different phases of the cell cycle was estimated in WL02 (left) and WL03 (right) using CellCycleScoring function in Seurat. (D) Gene set enrichment analysis (GSEA) pathways enriched by differentially expressed genes of tumour cells. Differentially enriched biological pathways are displayed ordered by the normalised enrichment score (NES).

Figure 3. CNV analysis of two liver metastases.

(A) Hierarchical clustering from inferCNV analysis showing CNV changes by chromosomes (columns) for individual tumour cells (rows). Blue indicates copy gains while red indicates copy losses. (B) LP-WGS analysis of two liver metastases. CNVs are denoted by horizontal lines indicating total or partial chromosomal losses (red) or gains (blue). (C) Clonality trees of each of tumour cells in the two liver metastases. The branches are scaled according to percentage of cells in the calculated subclone containing the indicated CNVs. (D) SNP array-based karyotyping of WL02.

Figure 4. Analysis of gene expression in two liver metastases.

(A) Immunohistochemical staining with BAP1 antibody in WL02, note the loss of nuclear staining in tumour cells (arrow) in the presence of positive internal control (retained nuclear staining) in endothelial and stromal cells (asterisk) (BAP-1 IHC, original magnification ×320). (B) Ridge plots of the 15-gene panel in tumour cells between WL02 and WL03. Red arrows indicate the direction of change in a Class 2 tumour.

A

Choroidal UM diagnosed in the left eye;

Biopsy performed for MLPA

Resection of the liver metastasis in segment III

Recurred liver metastasis identified by PET

More liver metastases identified by PET

The patient passed away

Week 0 160 165 202 246 253 255 256 259 266 267 272

Liver metastasis identified by PET

Enucleation of the left eye

Biopsy of the left lateral liver segment;

scRNA-seq, WGS and aCGH performed

Metastases in liver, bones and lymph nodes identified by PET

plaque brachytherapy

ipilimumab + nivolumab

nivolumab

B

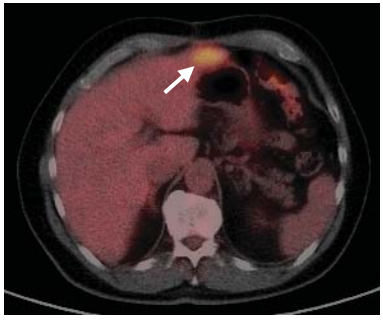

C

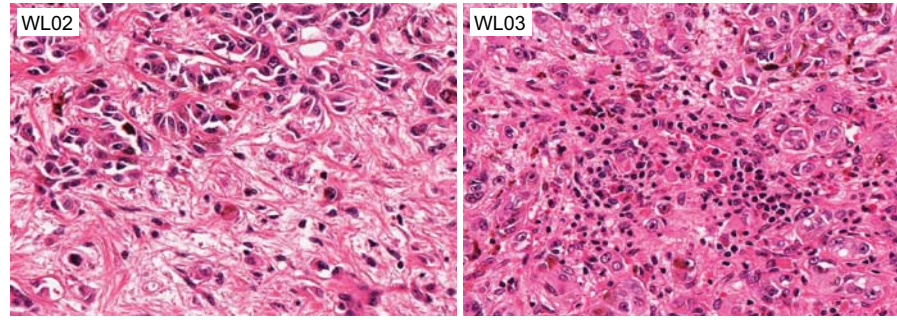

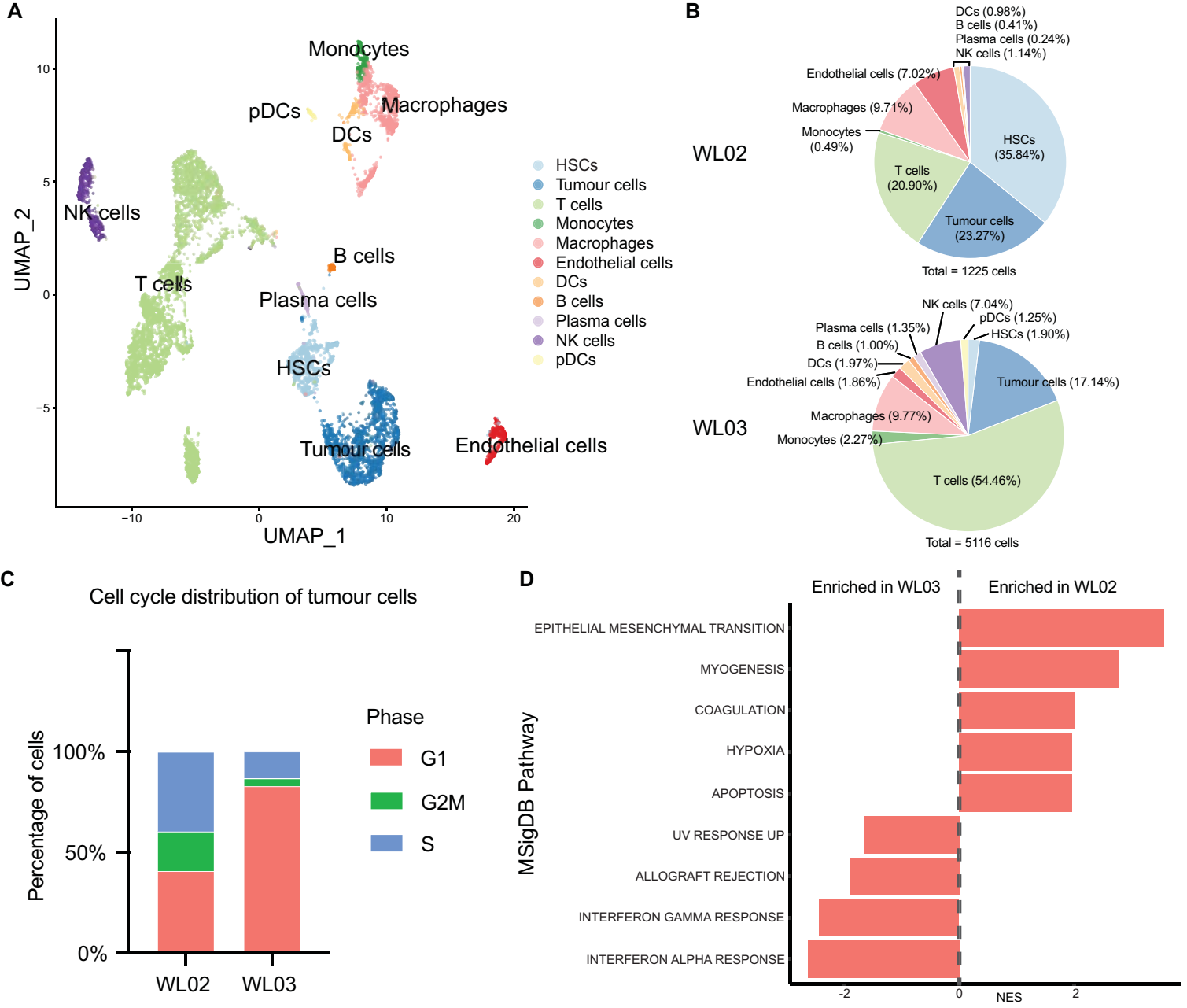
A
Monocytes
pDCs
Macrophages
DCs
NK cells
B cells
T cells
Plasma cells
HSCs
Tumour cells
Endothelial cells
UMAP_2
UMAP_1
HSCs
Tumour cells
T cells
Monocytes
Macrophages
Endothelial cells
DCs
B cells
Plasma cells
NK cells
pDCs
B
WL02
DCs (0.98%)
B cells (0.41%)
Plasma cells (0.24%)
NK cells (1.14%)
Endothelial cells (7.02%)
Macrophages (9.71%)
Monocytes (0.49%)
HSCs (35.84%)
T cells (20.90%)
Tumour cells (23.27%)
Total = 1225 cells
WL03
NK cells (7.04%)
pDCs (1.25%)
Plasma cells (1.35%)
HSCs (1.90%)
B cells (1.00%)
DCs (1.97%)
Endothelial cells (1.86%)
Tumour cells (17.14%)
Macrophages (9.77%)
Monocytes (2.27%)
T cells (54.46%)
Total = 5116 cells
C
Cell cycle distribution of tumour cells
Percentage of cells
100%
50%
0%
WL02
WL03
Phase
G1
G2M
S
D
Enriched in WL03
Enriched in WL02
MSigDB Pathway
EPITHELIAL MESENCHYMAL TRANSITION
MYOGENESIS
COAGULATION
HYPOXIA
APOPTOSIS
UV RESPONSE UP
ALLOGRAFT REJECTION
INTERFERON GAMMA RESPONSE
INTERFERON ALPHA RESPONSE
-2
0
2
NES

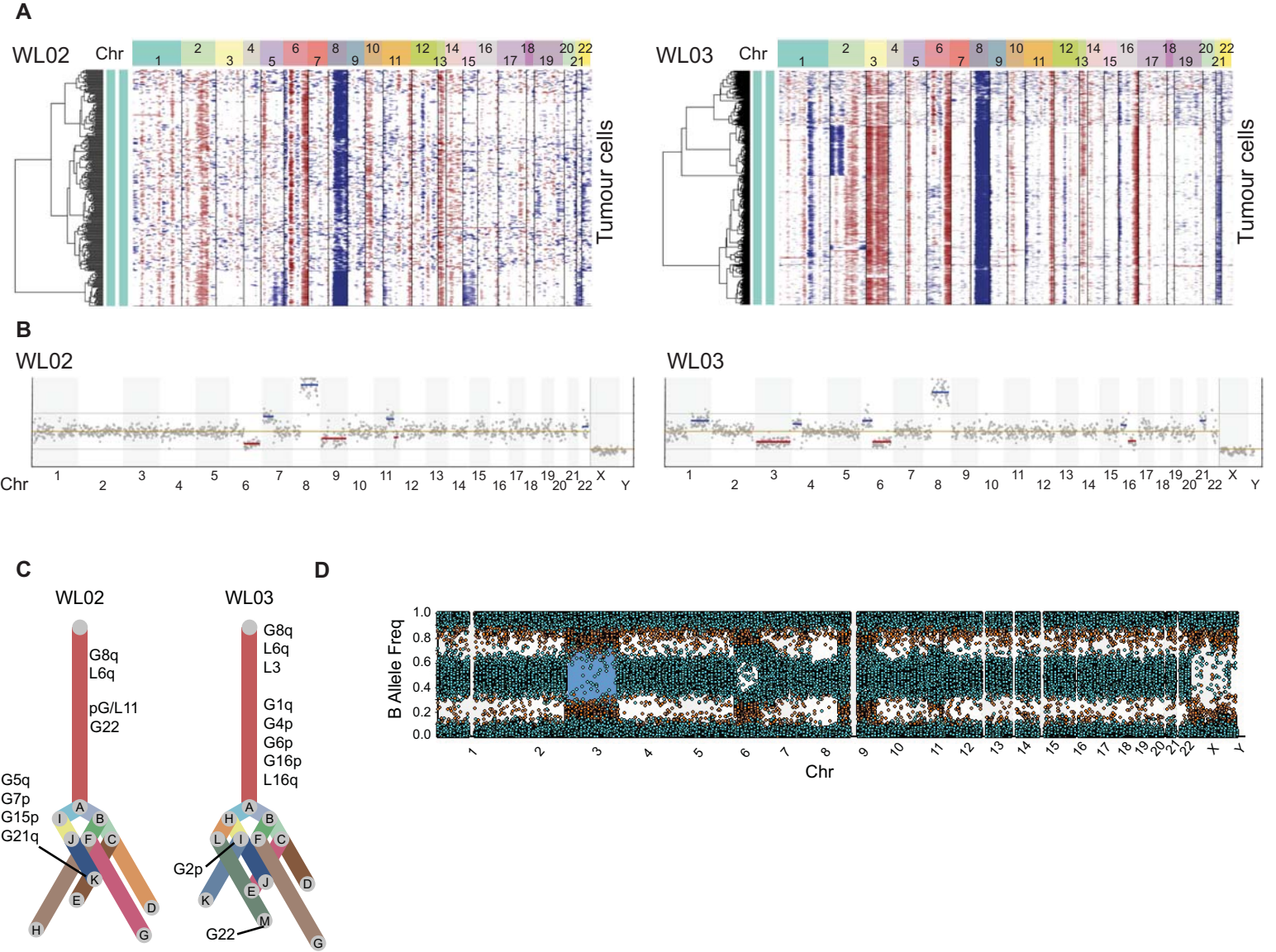
A
WL02
Chr
Tumour cells
WL03
Chr
Tumour cells
B
WL02
WL03
Chr
C
WL02
WL03
G8q
L6q
pG/L11
G22
G5q
G7p
G15p
G21q
G8q
L6q
L3
G1q
G4p
G6p
G16p
L16q
G2p
G22
D
B Allele Freq
1.0
0.8
0.6
0.4
0.2
0.0
Chr

A

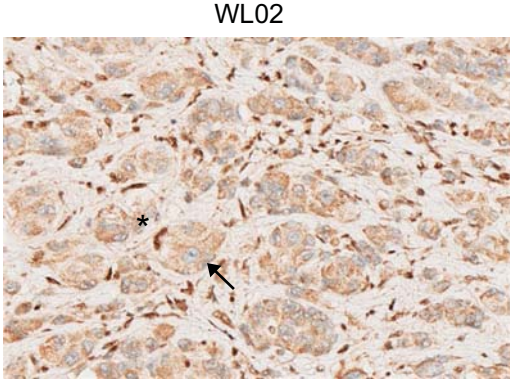
WL02
*

B

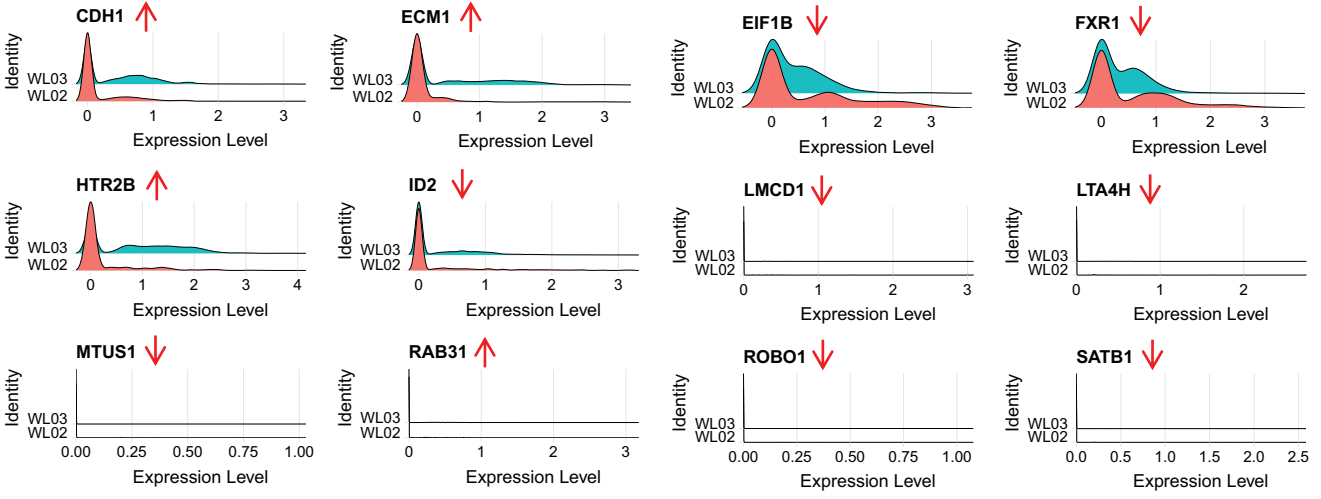
CDH1
ECM1
EIF1B
FXR1
HTR2B
ID2
LMCD1
LTA4H
MTUS1
RAB31
ROBO1
SATB1
Identity
WL03
WL02
Expression Level

Intra- and inter-tumoral heterogeneity of liver metastases in a patient with uveal melanoma revealed by single-cell RNA sequencing

Weitao Lin, Aaron B. Beasley, Nima Mesbah Ardakani, et al.

Cold Spring Harb Mol Case Stud published online September 1, 2021
Access the most recent version at doi:10.1101/mcs.a006111